Bulletin of the Seismological Society of America, Vol. 92, No. 8, pp. 3190–3209, December 2002

Site Effect Analysis around the Seismically Induced Ananevo Rockslide, Kyrgyzstan

by Hans-Balder Havenith, Denis Jongmans, Ezio Faccioli, Kanatbeck Abdrakhmatov, and Pierre-Yves Bard

Abstract In 1911, the surface-wave magnitude 8.2 Kemin earthquake hit northeastern Tien Shan (Kyrgyzstan), close to the cities of Bishkek and Almaty, the capitals of Kyrgyzstan and Kazakhstan, respectively. Several hundreds of people were killed by the earthquake, some by indirect effects such as landslides and mudflows. A particular but nonfatal landslide triggered by the Kemin event was a rockslide in the vicinity of Ananevo, north of lake Issyk Kul (Kyrgyzstan) rockslide located above the fault zone activated in 1911.

In the summer of 1999, a geophysical–seismological field trip was organized to study geology and to record seismic ground motions on and around the Ananevo rockslide. The work was part of project assessing seismogenic landslide hazard in northern Kyrgyzstan, based on various case studies of slope failures in connection with site-specific ground-motion dynamics.

The geophysical investigations consisted of seismic refraction tests processed as 2D seismic tomographies and surface-wave inversion, which were combined to build a 3D geophysical model of the landslide site. Ground motions from small earthquakes were analyzed using several techniques to define site effects over the mountain massif. Both H/V and standard spectral ratios indicated lower dominant frequencies with stronger amplification in the crest region with respect to the mountain slope. These effects could be partially simulated by 1D, 2D, and 3D finite-element modeling. By comparing the numerical results with the experimental data, the presence of a surficial low-velocity layer of varying thickness appeared to be the key factor controlling the ground motion around the rockslide.

Introduction

The mechanisms that lead to the static initiation of a landslide are often difficult to understand because of the complexity of local geology and lack of knowledge of about material properties. Extensive prospecting on the site and numerous back analyses are typically needed to define the factors inducing instability (McCann and Forster, 1990). The task becomes even more complicated if dynamic conditions are involved in the trigger processes because seismic ground motions depend on the specific source, path, and site characteristics. Evidence of such dependence is frequently met in seismically active mountain regions, such as the Tien Shan range in Central Asia (Fig. 1). During the last century, three earthquakes with magnitudes higher than M_s 7 triggered thousands of landslides of all sizes and types inside the Tien Shan range (Aitmatov *et al.*, 1997). One of them, the Ananevo rockslide located north of lake Issyk Kul in Kyrgyzstan, Central Asia (Fig. 1), was triggered by the M_s 8.2 Kemin earthquake in 1911 (Bogdanovich *et al.*, 1914). The earthquake caused many mudflows and rockslides, particularly in Chilik-Kemin and Chon Aksu valleys close to the surface ruptures of the activated fault segments (Bogdanovich *et al.*, 1914; Delvaux *et al.*, 2001). Inside the epicentral zone (Fig. 1), the seismically triggered Kemin rock avalanche buried a village of yourts with some tens of people killed. The global loss of lives related to the earthquake amounts to several hundreds of people (Bogdanovich *et al.*, 1914).

This study focuses on the local ground-motion factors that could have influenced the triggering of the Ananevo rockslide (Figs. 1, 2), which affected a hill of a few hundred meters high. This site was chosen for its simple morphology (N–S oriented hill) and geological conditions (homogeneous granite massif). In order to assess the local geological conditions and to understand the dynamic response of the site, a two-month seismological and geophysical–geological survey was organized on and around the Ananevo rockslide. Seismic methods were used to investigate the site and to construct a rough 3D model composed of seismic layers with

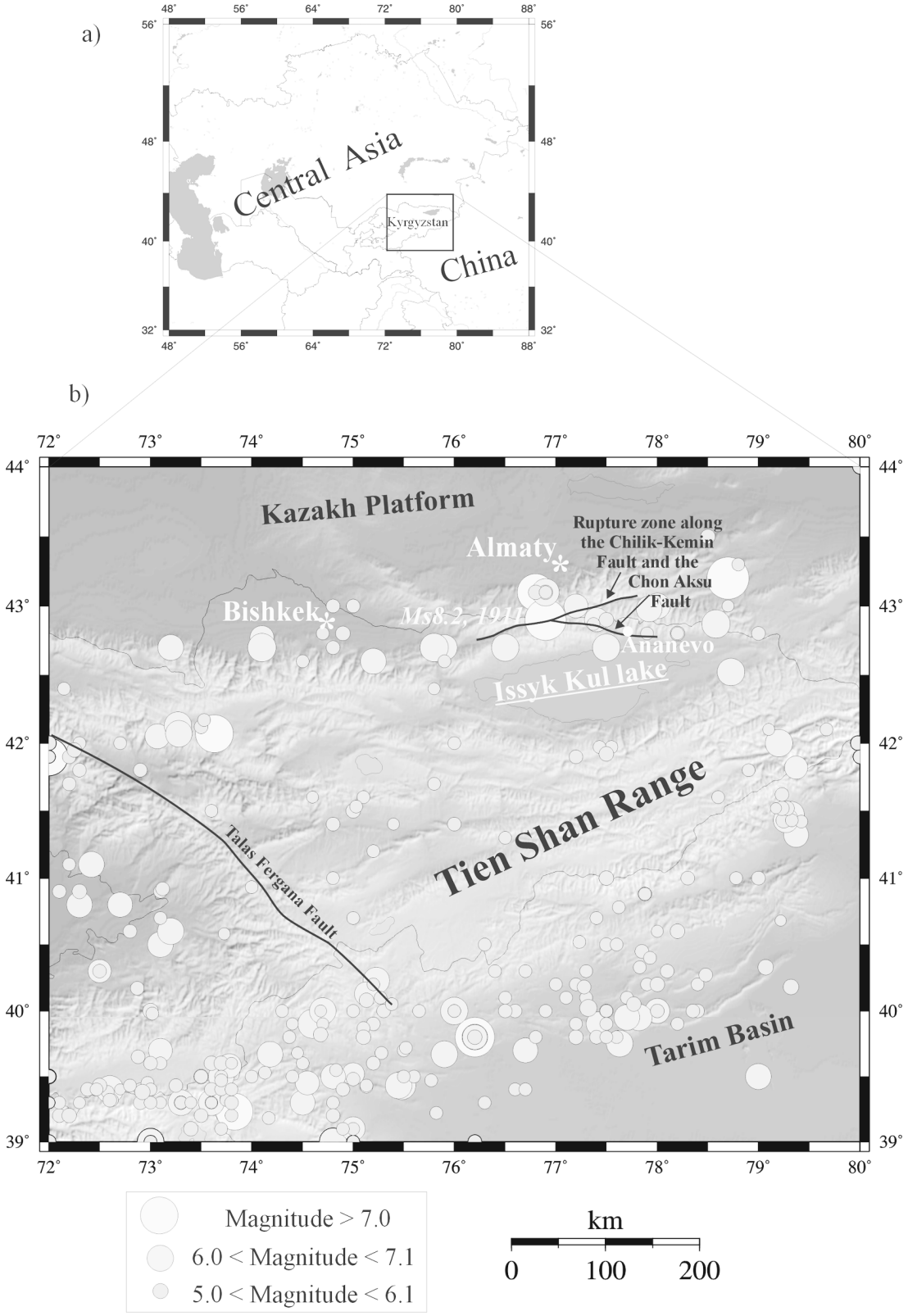

Figure 1. (a) Location of Kyrgyzstan. (b) Map showing the morphology of the central-eastern Tien Shan, the central part of the Talas Fergana fault, and the Chilik-Kemin and Chon Aksu faults. Epicenters of instrumental and historical earthquakes in a magnitude range between 5 and 8.3 are indicated by a circle.

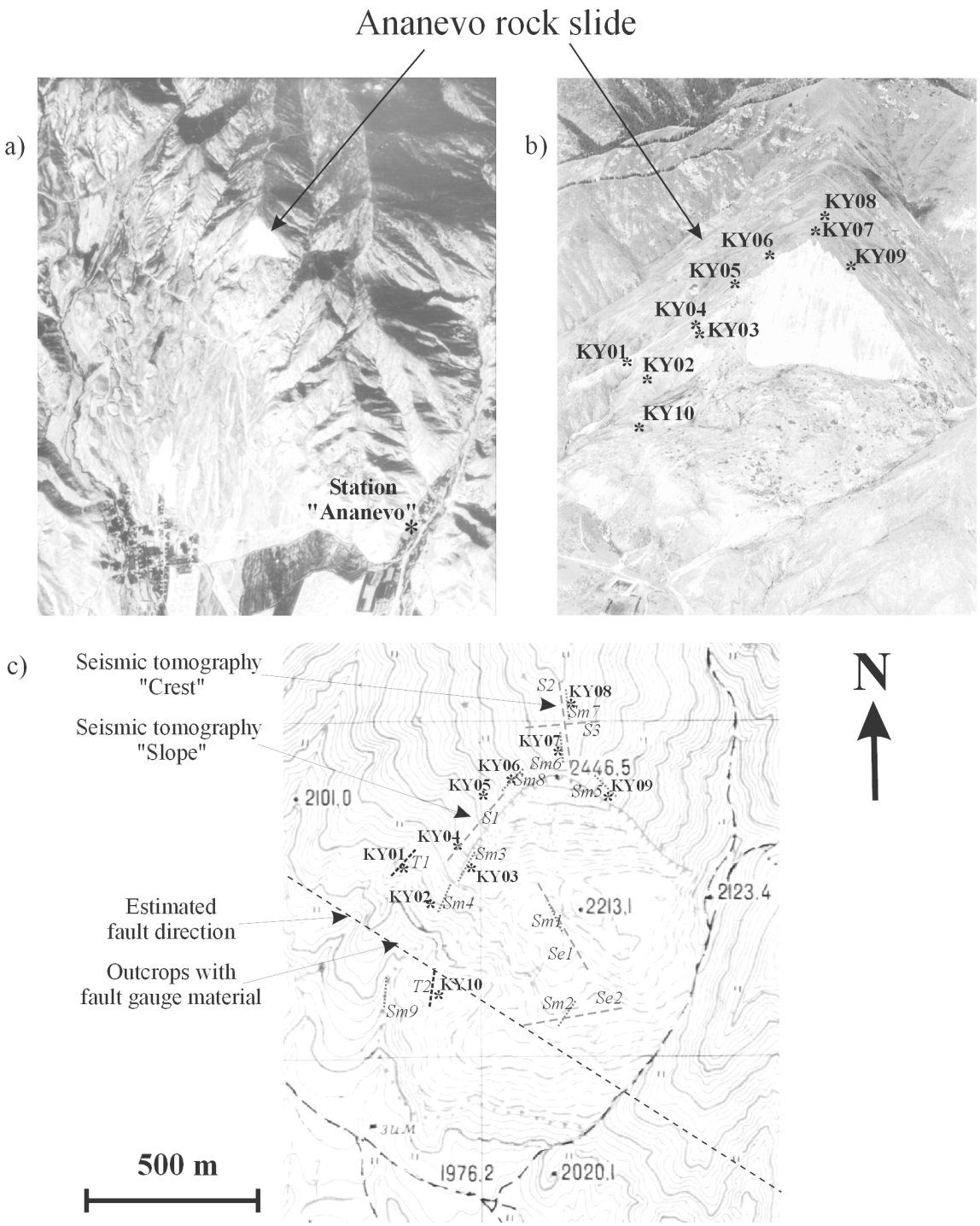

Figure 2. (a) 3-m resolution satellite image of the Ananevo rockslide (200-m-high scarp marks scale) site with location of Ananevo seismological station (American network). (b) Helicopter Photograph (Torgoev, Jirmolov) of Ananevo rockslide with location of seismic stations KY01 to KY10. (c) Map of the landslide with location of seismological stations KY01 to KY10 and location of seismic profiles. Profiles S1–S3: 115-m profiles with five explosive sources (central, direct/reverse 20-m offsets, and 50-m offsets). Profiles Sm1–Sm8: 69- to 92-m sledgehammer profiles, central shot and direct/reverse 0-m offsets. Profiles T1 and T2: 92-m sledgehammer profiles with shots at all 24 geophones. Profiles Se1 and Se2: 115-m profiles with one direct 180-m offset shot. Long dashed line corresponds to the estimated fault direction.

varying seismic velocities and quality factors. This model has then been used to simulate dynamic ground motions that have been compared with experimental data obtained by the seismological survey.

The present article constitutes the basis of an extensive work on numerical modeling of dynamic effects on slopes that cannot be fully developed here. In order to allow the reader to gain insight into the general goal of the study, it will also be referred to further analyses, which are more focused on the seismic slope stability aspects.

Seismotectonic Context of the Tien Shan

The Tien Shan is a high, intracontinental mountain belt in Central Asia, with an E–W extension of about 2500 km and a maximum width of more than 500 km. It culminates in the 7453-m-high Peak Pobedi in eastern Kyrgyzstan. The Kyrgyz Tien Shan is bounded to the north by the stable Kazakh platform (Avouac *et al.*, 1993) (Fig. 1b) and to the south by the Tarim basin. The structure of the Tien Shan is characterized by alternating, roughly E–W trending, mountain ranges and intramontane basins. Palaeozoic rocks and older basement constitute the core of the ranges, whereas the basins are filled by Cenozoic and Mesozoic sediments and are mostly bounded by oppositely vergent thrust faults (Cobbold *et al.* 1996). Other structural features are strike-slip faults, the most prominent one being the NW–SE trending Talas-Fergana fault (see its central part in Fig. 1), having a total dextral offset, since the Permian, of about 200 km. Thrust and strike-slip faults accommodate a roughly N–S shortening of 10–30 mm/yr (Abdrakhmatov *et al.*, 1996; Reigber *et al.*, 1999) throughout this intracontinental mountain belt.

Due to its tectonic activity, the Tien Shan is prone to high seismicity. In the last century, several strong earthquakes struck the region (Fig. 1b), such as the cited M_s 8.2 Kemin earthquake in 1911, the M_s 7.6 Chatkal earthquake in 1946, and the M_s 7.3 Suusamyr earthquake in 1992 (Gomez *et al.*, 1997; Mellors *et al.*, 1997).

Geological Setting

The rockslide of Ananevo is located in the Kungey range (Fig. 1), northeastern Tien Shan, which is principally made of paleozoic sedimentary and magmatic rocks (Akad Nauk Kirghiz S.S.R. and Ministry of Geology, 1980) and is delimited in the south by the Issyk Kul basin and in the north by the Kazakh platform. Inside the range, several faults are seismically active and likely to produce catastrophic seismic events of magnitudes greater than 7 within a return period of less than 1000 years (Imanbekov *et al.*, 1999). The most seismically active faults are the ENE–WNW trending Chilik-Kemin fault and WNW–ESE trending Chon Aksu-fault, both activated in 1911, with surface rupture over a total length of about 250 km (Fig. 1). The rupture indicates different kinds of fault mechanisms combining thrusting and sinistral strike slip (Delvaux *et al.*, 2001). Maximum displacements observed along the fault trace after the Kemin earthquake amount to 5–8 m. Some scarps show apparent vertical displacements of more than 15 m, but recent trench exploration and geophysical data (Delvaux *et al.*, 2001) have shown that these displacements should be related to at least three different shocks.

The N–S oriented Ananevo rockslide is situated along the Chon Aksu fault segment at 70 km to the east of the epicentral zone. The location and WNW–ESE trend of the fault trace could be defined, respectively, by an outcrop of fault gauge material (Fig. 2) and by a clear fault scarp at 3 km to the west of the site. The width of the fault zone activated in 1911 is, however, not exactly known. The south-facing rockslide scarp is 200 m high, with a total height from toe to crown of about 500 m and a total length of 900 m (Fig. 2). The components of the tongue are of variable sizes from fine-grained arenites up to house-scale blocks with low cohesion.

Geophysical–Seismological Exploration Methods

The geophysical survey consisted of seismic refraction tests with explosives or a sledgehammer as energy sources. The seismic waves were recorded by 24 4.5-Hz geophones connected to a 16-bit seismograph and aligned along a profile with a maximum length of 115 m. Two 115-m profiles with one explosive source at 180-m offset were performed on the tongue (Fig. 2c). These data were analyzed by classical seismic refraction processing (Burger, 1992). Three 115 m-profiles with five explosive sources, one at the profile center, two at 20-m offset, and another two at 50-m offset to each side of the profile were carried out on *in situ* rock at the mountain crest and along the slope (Fig. 2c). Ten sledgehammer profiles of 69- to 92-m length with three source points, at the center and at each profile end, were also performed all over the site. At some places, 24 sledgehammer source points were used to get a better resolution of underground heterogeneities. All the profiles on *in situ* rock, with explosives or a sledgehammer, were interpreted as 2D *P*-wave refraction tomographies using the SARDINE software (Demanet, 2000). The same seismic data were also processed by surface-wave inversion (Herrmann, 1987) to obtain the corresponding *S*-wave velocity (Vs) models.

Earthquake ground motions were recorded during seven weeks by 10 CMG-40 receivers connected to RefTek stations (see location in Fig. 2). Measurements were continuous at a frequency of 250 Hz and with 16-bit amplitude resolution. Additional noise recordings were performed with a L5s receiver connected to a RefTek station. Seismological data of a permanent RefTek station (added recently to the Kyrgyzstan Network by Pavlis *et al.* [2000]) located 8 km north of Ananevo and 2.5 km southeast of the landslide site were also used. The seismometer is a broadband L3, and recordings are continuous at 20 Hz (periodically 40 Hz) with 16-bit amplitude resolution.

A total of more than 80 local and regional events were recorded during the experiment time, but only 37 of them with surface-wave magnitudes between 0.5 and 3.0 were located by the Kyrgyz network (Table 1, Fig. 3). Another 30 regional and teleseismic events were detected, and 13 of them are indexed in the world seismic catalog (Table 1, Fig. 3). Most of them are located in the southern Tien Shan–Pamir region and have magnitudes between 3.9 and 5.5. The Izmit earthquake (M_s 7.8) of 17 August 1999 was also recorded.

Unfortunately not all 110 events have been recorded at all stations because of practical problems such as battery supply and memory depletion. Because recording was continuous, a large amount of noise measurements is available for site effect assessment at all locations.

Geophysical Results

Figure 4 shows two examples of *P*-wave refraction tomography sections performed on the crest and along the slope 50 m west of the rockslide (see Fig. 2 for location). Maximum investigation depth along these 215-m profiles (including 50-m offsets) is about 55 m. On the crest (Fig. 4a), *P*-wave velocities (Vp) are particularly low, with 900 m/sec at a depth of 35 m. Along the slope, the same Vp was obtained at a depth of 15 m (Fig. 4b). Vp of more than 1500 m/sec that may indicate the presence of the water table appear at the crest at the limit of investigation depth (greater than 50 m); along the slope, the depth of the water table might be estimated at about 50 m (Fig. 4).

To all seismic data, we also applied the surface-wave inversion technique (Herrmann, 1987) in order to determine Vs and quality factors (Qs) over depth. On the crest, surface-wave inversion determined Vs of 250 m/sec, 400 m/sec, and 600 m/sec at a depth of 0 m, 20 m, and more than 35 m, respectively. Similar results were obtained all around the landslide site, with somewhat higher Vs along the slope and at the bottom of the hill than at the crest. Close to surface, the quality factor Qs was generally less than 15 increasing up to 50 at a maximum resolved depth of 30 m.

The measured seismic velocities are amazingly low for granite rocks outcropping at numerous sites along the hill. These low values suggest a high fracturing and weathering degree of the massif. Ultrasound *in situ* measurements on decimeter-scale blocks and laboratory ultrasound analyses on centimeter-size rock samples have shown Vp of 1800 m/sec and 5500 m/sec, respectively. The decrease of acoustic velocities with increasing block size is probably linked to small-scale fracturing. Over and beyond that, Vp values along the seismic profiles are generally less than 600 m/sec close to surface, that is, much lower than 1800 m/sec obtained at decimeter scale. This difference may be attributed to the medium-size and large-size fractures that are also observed at many outcrops around the rockslide and inside the landslide scarp.

Besides the scale-dependent velocity change, the thickness of surficial low-velocity layers increases from bottom to top of the hill, in relation with the stronger weathering and fracturing at the mountain crest with regard to its slope and foot.

The two large seismic profiles (Se1 and Se2 on map in Fig. 2c) performed on the displaced material allowed estimating the thickness of the tongue at about 65 m in its central part. Below this depth, refraction tests indicate the presence of thick weathered rock with Vp between 2000 and 2300 m/sec. At a depth of 120 m to 130 m, the two profiles detect the granite bedrock (Vp from 5600 to 5800 m/sec).

By combining all the geophysical data, a 3D seismic model composed of three weathered layers and the underlying bedrock has been developed, whose characteristics are given in Table 2.

Since the rupture occurred in 1911, no topographical data of the site are available before the landslide. Therefore, on the basis of the present geophysical model and of the evaluation of the displaced volume along a sliding surface, a 3D model previous to failure has been constructed (Fig. 5). Inside this model, three sections (labeled 1–3 in Fig. 5b) have been drawn for numerical modeling. Cross sections 1 and 2 located outside the slide are common to the models prior to and after failure.

Analysis of Ground-Motion Data

Seismograms and Spectrograms

Ground-motion data were used to assess the occurrence of possible topographic amplification effects around the rockslide. Seismograms (N–S component) of two regional (event 29/7/99, distance of 335 km and azimuth of N278°E; event 16/8/99, distance of 437 km and azimuth of N241°E, see Table 1) and two local earthquakes (events 2/8/1999 and 7/8/1999) are shown in Figure 6. Inspection of these recordings reveals that the investigated site amplifies the ground motion by a factor of 2–5 (for peak amplitudes) with respect to the site of the Ananevo permanent station, which is considered as a reference station. Maximum amplitudes are generally obtained for the stations close to the crest (KY08 and KY07) and at station KY02 in the lower part of the slope. In Figure 7 are shown seismograms (N–S component) and respective spectrograms for a local event (20/7/1999) measured at site REFE (permanent Ananevo station, Fig. 7a) and sites along the slope of the landslide mountain (Fig. 7b–g). Spectrograms were calculated using the maximum entropy spectral estimator method (Lacoss, 1971), with a sliding window of 0.6 sec and a data slice interval of 0.4 sec. They are normalized for each signal with varying amplitude scales from one signal to another. Most remarkable are the strong amplitudes and long durations of signals at the mountain crest (stations KY07 and KY08). Post *S*-wave energy maxima at low frequencies (less than 5 Hz) are typically observed at

Table 1
List of the Earthquakes Recorded by the Temporal Network and Located by the Kyrgyz Network

Year	Month	Day	Hour	Minutes	Seconds	Lat °N	Lon °E	Depth (km)	Magnitude	Type	Epicentral Distance (km)
1999	7	5	20	26	56.60	42.68	75.38	24.1	1.6	M_s	264
1999	7	6	5	8	52.19	40.84	79.90	33.0	4.5	m_b	461
1999	7	6	20	29	31.44	41.76	73.98	4.5	1.1	M_s	464
1999	7	7	6	25	2.02	43.23	77.34	0.2	1.5	M_s	78
1999	7	8	9	38	10.81	43.07	74.92	4.1	1.7	M_s	320
1999	7	10	8	15	29.53	40.97	72.69	7.2	1.5	M_s	659
1999	7	11	18	12	37.05	42.19	73.49	4.9	1.1	M_s	497
1999	7	13	0	40	40.89	42.15	73.68	14.0	2.6	M_s	477
1999	7	15	21	47	9.65	37.47	72.50	71.0	4.9	m_b	1097
1999	7	15	22	47	43.17	40.39	71.10	33.0	4.5	m_b	869
1999	7	16	8	52	25.84	42.77	75.86	6.7	0.8	M_s	206
1999	7	16	10	14	44.03	43.12	74.62	7.0	2.5	M_s	356
1999	7	18	1	15	33.69	42.78	75.91	8.2	1.3	M_s	200
1999	7	18	21	51	49.35	37.34	72.32	33.0	4.9	m_b	1128
1999	7	21	17	28	45.10	42.58	75.08	17.0	1.5	M_s	301
1999	7	25	16	53	14.53	44.56	80.88	10.0	4.3	m_b	500
1999	7	28	13	17	12.47	30.00	69.40	33.0	5.5	M_w	2445
1999	7	29	8	4	2.50	42.70	74.78	12.7	1.5	M_s	335
1999	7	29	8	35	19.13	40.10	71.12	33.0	4.7	m_b	892
1999	7	29	20	44	34.21	43.57	76.44	7.0	1.3	M_s	188
1999	7	30	15	34	52.85	41.52	75.26	10.7	1.8	M_s	352
1999	7	31	1	52	52.26	42.59	75.11	14.1	2.0	M_s	298
1999	7	31	7	13	4.97	43.34	75.00	7.0	1.2	M_s	320
1999	8	1	14	35	40.07	41.57	73.27	7.4	2.2	M_s	554
1999	8	1	20	5	52.34	42.27	74.85	5.1	1.2	M_s	338
1999	8	2	18	27	39.64	41.90	76.95	0.1	1.4	M_s	170
1999	8	2	19	2	3.06	41.87	76.99	0.1	1.0	M_s	173
1999	8	3	0	37	34.57	41.94	76.90	0.0	2.0	M_s	167
1999	8	3	10	33	59.40	42.31	73.71	5.4	0.9	M_s	468
1999	8	4	0	9	0.54	37.39	86.88	33.0	5.1	M_w	1710
1999	8	4	3	21	13.12	41.07	74.06	0.1	2.2	M_s	512
1999	8	5	22	59	7.60	41.90	76.94	0.0	1.0	M_s	171
1999	8	6	8	5	37.22	42.36	72.92	0.1	1.1	M_s	557
1999	8	6	15	34	27.03	41.05	74.02	0.0	1.2	M_s	518
1999	8	7	17	31	16.42	42.71	76.15	17.0	1.0	M_s	172
1999	8	9	11	47	6.30	42.25	76.30	15.4	1.3	M_s	179
1999	8	10	11	21	36.94	42.11	76.79	19.9	1.3	M_s	150
1999	8	11	20	34	16.58	39.11	79.18	33.0	4.4	m_b	696
1999	8	12	9	2	33.18	43.06	74.91	3.0	1.3	M_s	321
1999	8	12	13	20	43.63	41.95	76.62	8.0	1.0	M_s	184
1999	8	13	1	20	59.31	42.30	77.92	0.3	1.3	M_s	97
1999	8	16	22	32	39.73	41.39	74.52	12.1	2.5	M_s	437
1999	8	17	0	1	39.13	40.75	29.86	17.0	7.8	M_s	4683
1999	8	18	4	48	2.30	42.09	75.92	15.5	2.4	M_s	232
1999	8	18	14	1	33.62	42.42	72.85	12.0	1.1	M_s	564
1999	8	18	22	37	20.69	43.71	76.62	5.4	1.2	M_s	191
1999	8	19	20	46	58.49	39.28	69.19	33.0	4.5	m_b	1155
1999	8	21	6	19	16.58	44.61	84.68	33.0	3.9	m_b	937
1999	8	21	0	9	7.77	36.52	70.60	162.0	4.5	m_b	1358
1999	8	21	1	57	7.57	41.41	75.27	19.6	1.6	M_s	363

the crest (stations KY07 and KY08) and to a lesser extent at stations KY02 and KY04. The variation of the energy maximum with time and frequency suggests the presence of trapped surface waves (Jongmans and Malin, 1995), which cause the low-frequency waves to last longer than high-frequency waves (Fig. 7g).

Site Effect Assessment

The computation of the ratio of the horizontal to vertical components (H/V) at one station and the standard spectral ratios (SSRs) between two stations are now common methods for studying site effects (see, for instance, Field and Jacob [1995] and Borcherdt [1970]; for a definition of the

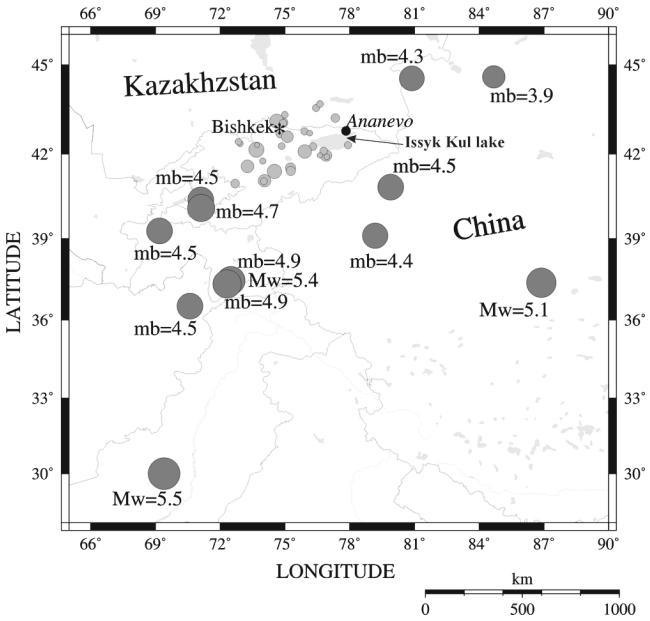

Figure 3. Location of events recorded by the summer 1999 seismological survey at the Ananevo rockslide. Light gray circles, events located by Kyrgyz network; dark gray circles, events located by other networks (world seismic catalog).

techniques). SSRs were calculated by dividing the 10%-smoothed ground-motion spectra at the specific site by the 10%-smoothed spectra of the reference site (station Ananevo, REFE) following the smoothing procedure proposed by Riepl *et al.* (1998). Both SSR and H/V ratios were calculated extracting 15-sec *S*-wave and 20-sec coda windows for regional events. H/V ratios were also applied to 20-sec noise windows and calculated according to Nakamura (1989).

Figure 8 presents the H/V ratios computed for the three wave types and the two horizontal components (N–S and E–W) at the stations REFE and KY08. The number of considered signals varies between 39 and 108, and the mean ratios are shown with the plus/minus one standard deviation curves. First, the ratio shapes along the N–S and E–W directions are quite similar, although the amplitude is slightly and systematically lower for the E–W component. Second, H/V ratios for the different wave types appear remarkably stable, both in terms of amplitude and frequency range. The same result has been obtained at the other stations. At station KY08, H/V ratios along the N–S component exhibit a peak of 4–5 (3–4 for the component) in a frequency range between 1 and 2 Hz. Maximum H/V amplitudes are lower (2 to 3) at station REFE in a bandwidth from 1.5 to 4 Hz. This site can therefore not be considered as a pure reference station, though it is located on granitic rock. In a way similar to the sites around the rockslide, a shallow weathered layer probably amplifies the signal. However, the H/V results indicate that this station exhibits the lowest amplitude and thus will be considered as local reference in the following.

Figure 9 displays, for four stations (KY01, KY04, KY06 and KY08) around the rockslide, detailed SSR data (for each event) and mean SSR plus/minus one standard deviation (Fig. 9a,c,e,g) for the N–S and E–W components. All four stations reveal strong deviations of single SSR from the mean ratio. Nevertheless, clear amplified frequency ranges can be distinguished: amplification factor of 3 at 2–3 Hz for station KY01 and amplification factors of 5, 8, and 7 at 1–2 Hz for stations KY04, KY06, and KY08, respectively.

Because station REFE exhibits some amplification effects, we tested the stability of SSR by using a second reference station (KY10), which is located at the foot of the slope. For the same four stations, the mean SSR ratios using KY10 and REFE as references are compared (Fig. 9b,d,f,h). In the same figures are also plotted the H/V ratios for *S* waves and coda. SSR values computed with station KY10 are always lower than H/V and SSR values using station REFE. This results from amplification effects at station KY10 itself that are higher than the site effects at REFE (see SSR amplification with respect to REFE of 1–4 in Fig. 10). The mean SSR using REFE as reference station are given in Figure 10 for all the other stations, including KY10. Amplification at the latter station is higher than 2, regardless of the frequency. The comparison between H/V ratios and SSRs (with REFE) shows that H/V ratios are similar to or lower than SSRs (Fig. 9). The H/V ratios and SSR are most consistent at frequency values lower than the fundamental resonance frequency. Above the resonance frequency, SSRs may be 3 times higher than H/V values, especially for stations close to the mountaintop. In most cases, H/V ratios can be considered as lower bound on the amplification. The SSR distribution along the slope west of the landslide is displayed in Figure 10 for the N–S and E–W components. All sites are amplified by a factor of at least 4 with regard to the reference station REFE. The strongest amplification (over 7) occurs close to the crest region in a frequency range between 0.8 and 2.5 Hz, with a maximum of 10 at 1.25 Hz for station KY07. Downhill, the fundamental frequency increases and the maximum amplification appears between 2 and 3.5 Hz at the foot of the mountain (between stations KY01 and KY10). An interesting feature is the narrow amplified frequency range at station KY05 with respect to neighboring stations, which probably results from local heterogeneities of site characteristics.

Numerical Modeling of Site Effects

In order to understand the observed ground-motion variations over the landslide site, dynamic numerical modeling was performed with a 2D and 3D viscoelastic code based on Legendre polynomial approximations. The code implements a hybrid method (Faccioli *et al.*, 1997) combining low-order finite elements (FEs) and high-order spectral elements (SEs). On one side, triangular FEs facilitate meshing of complicated geometries. On the other side, for the same frequency content of propagating waves, the highly accurate quadrilateral SEs allow use of a coarser mesh (2–3 nodes per wavelength)

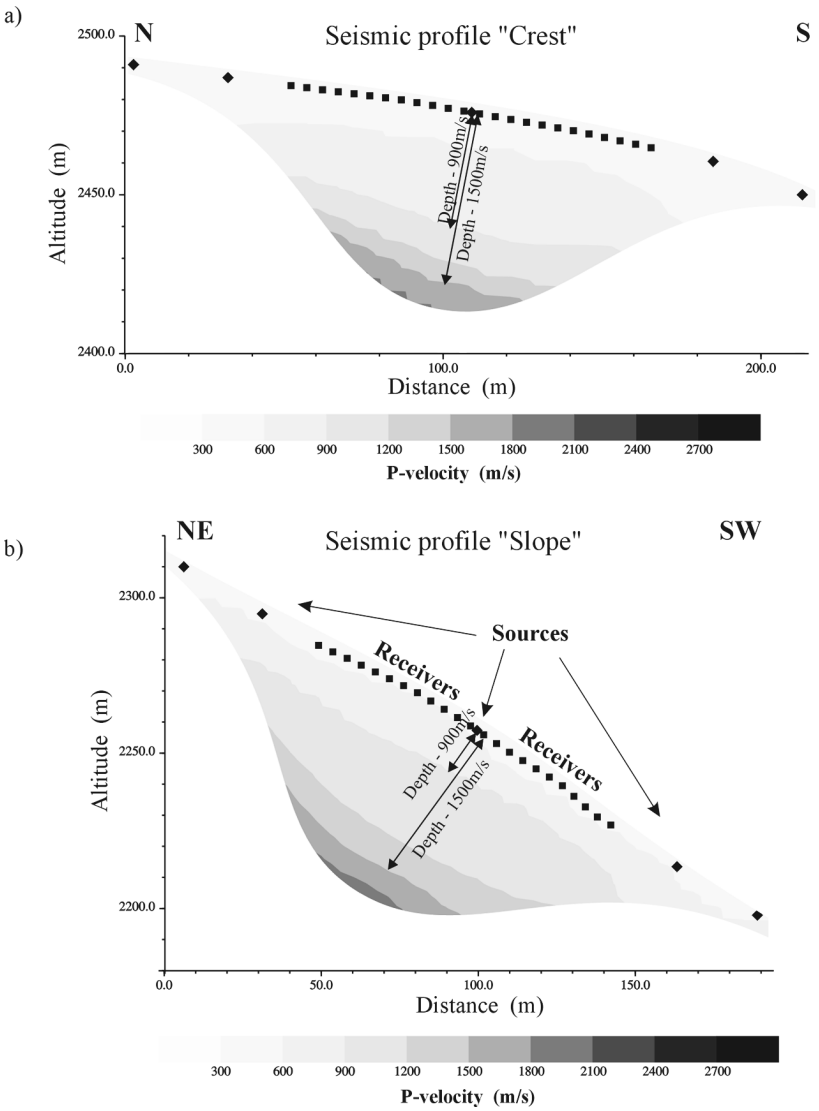

Figure 4. (a) *P*-wave refraction tomography (profile Crest, S1 in Fig. 2c) along the crest with position of five sources (diamonds) and 24 geophones (squares). (b) *P*-wave refraction tomography (profile Slope, S2 in Fig. 2c) along the southwestern slope with position of five sources (diamonds) and 24 geophones (squares). Arrows indicate the depth of Vp = 900 m/sec and Vp = 1500 m/sec layers.

Table 2
Dynamic Characteristics of the Four Seismic Layers Determined from Geophysical Prospecting

Layer	Vp (m/sec)	Vs (m/sec)	Qs	Ed (Pa)	ν	Density*
1	800	400	35	7.78e + 08	0.33	1.80
1′	1143	600	35	1.79e + 09	0.31	1.90
2	1700	910	150	4.29e + 09	0.30	2.00
3	3950	2180	400	2.81e + 10	0.28	2.30
Bedrock	6000	3470	600	7.95e + 10	0.25	2.65

*Density values were estimated from *in situ* observations.

with respect to FEs (8–10 nodes per wavelength). The application of both types of elements makes it possible to model complex site conditions with relatively low calculation costs by using a refined FE mesh embedded in a coarser SE mesh. The principal condition linking the two meshes is that all SE nodes at the FE-SE interface coincide with a FE node; the opposite is not necessary.

The 2D numerical simulations were performed with two types of models—homogeneous bedrock and bedrock overlaid with surface layers (see Table 2 for characteristics)—built for two sections across the geophysical 3D model (cross section 1 and cross section 2, see Fig. 5). Cross sections 1 and 2 are oriented along a NE–SW and E–W direction, respectively. Surface layers, if included in the model,

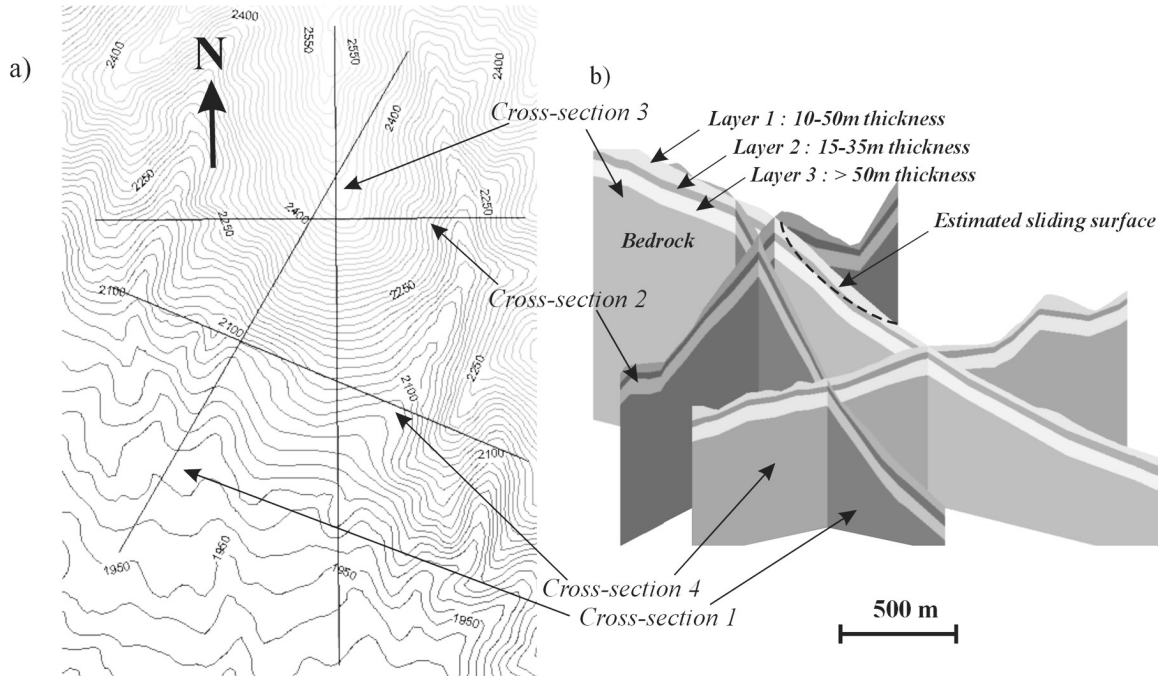

Figure 5. Topographical map (prior to failure) showing location of sections. (b) Cross sections 1, 2, 3, and 4 across the geophysical model previous to failure. Location of layers 1, 2, and 3 as well as the estimated sliding surface along section 3 are indicated.

were meshed with FEs, whereas the underlying bedrock was meshed with SEs. Sources were introduced along a horizontal line at the bottom of the model (input option of the code) in order to produce vertically propagating *SH* plane waves. The source function was a vertically incident 2 Hz Ricker wavelet. Figure 11 shows simulated time histories and SSR distributions obtained at the surface for the four described model types: cross sections 1 and 2 with homogeneous bedrock (Fig. 11a,b) and with bedrock and surface layers (Fig. 11c,d). Along the two sections, a reference receiver on the bedrock has been selected at 2 km southwest of the slope in cross section 1 and at 2 km west of the mountain slope in cross-section 2, in both cases on a flat surface. The simulated "reference signal" was also used for the respective sections with surface layers. In the homogeneous case, only a slight amplification at the crest can be observed on the signals along section 1 (Fig. 11a). In terms of SSR, the maximum spectral amplification is about 2 at a low frequency of 0.5 Hz. Along section 2 with homogeneous bedrock (Fig. 11b), signals are slightly amplified at the crest, without any enhanced duration. SSR distributions show an amplification of 1–2 between 0.2 and 5 Hz with a maximum factor slightly higher than 2 at 3.8 Hz. On the other hand, SSR distributions along both sections 1 and 2 with homogeneous bedrock indicate significant deamplification of the signals along the mountain slope for frequencies higher than 1–2 Hz.

The introduction of surface layers in both sections involves the generation of site effects with large amplitudes and signal duration (Fig. 11c,d). Strongest amplifications are simulated at the top of the mountain slope (station KY07) in cross section 2, perpendicular to the crest. These characteristics are highlighted by the distribution of theoretical SSR showing amplification factors higher than 10 at 1.4 Hz close to the crest (Fig. 11d) and the development of diffracted surface waves propagating in the upper layers. Along cross section 1 with bedrock and surface layers, an amplification of 6–8 occurs both at the crest and over convex regions along the slope (Fig. 11c) for frequencies rising from 1.8 Hz at the crest to 2.4 Hz at the bottom of the slope. This last feature was observed on experimental data (Fig. 10b). In cross section 2 (E–W profile), a high amplification (over 10) is obtained at the crest for a frequency of 1.2–1.7 Hz. Both amplification and frequency ranges are similar to the observed ones (compare Fig. 10 and 11d), whereas the amplified frequency range of 1.5–2 Hz along cross section 1 (NE–SW) is clearly higher than the experimental one. In cross section 2, variation of the fundamental frequency along the slope is much stronger than in cross section 1: 1.3 Hz at the crest to 4 Hz at the foot of the mountain where slight deamplification occurs in the lower frequency range.

The completed 2D simulations reveal the need of introducing surface layers into the models in order to understand observed amplifications. Taking into account topography only clearly proved to produce unsatisfactory results. Similar discrepancies between theoretical and experimental results have been observed many times (e.g., Bouchon and Barker, 1996; Paolucci *et al.*, 1997). 2D modeling was, however, unable to explain some features, such as the general form of

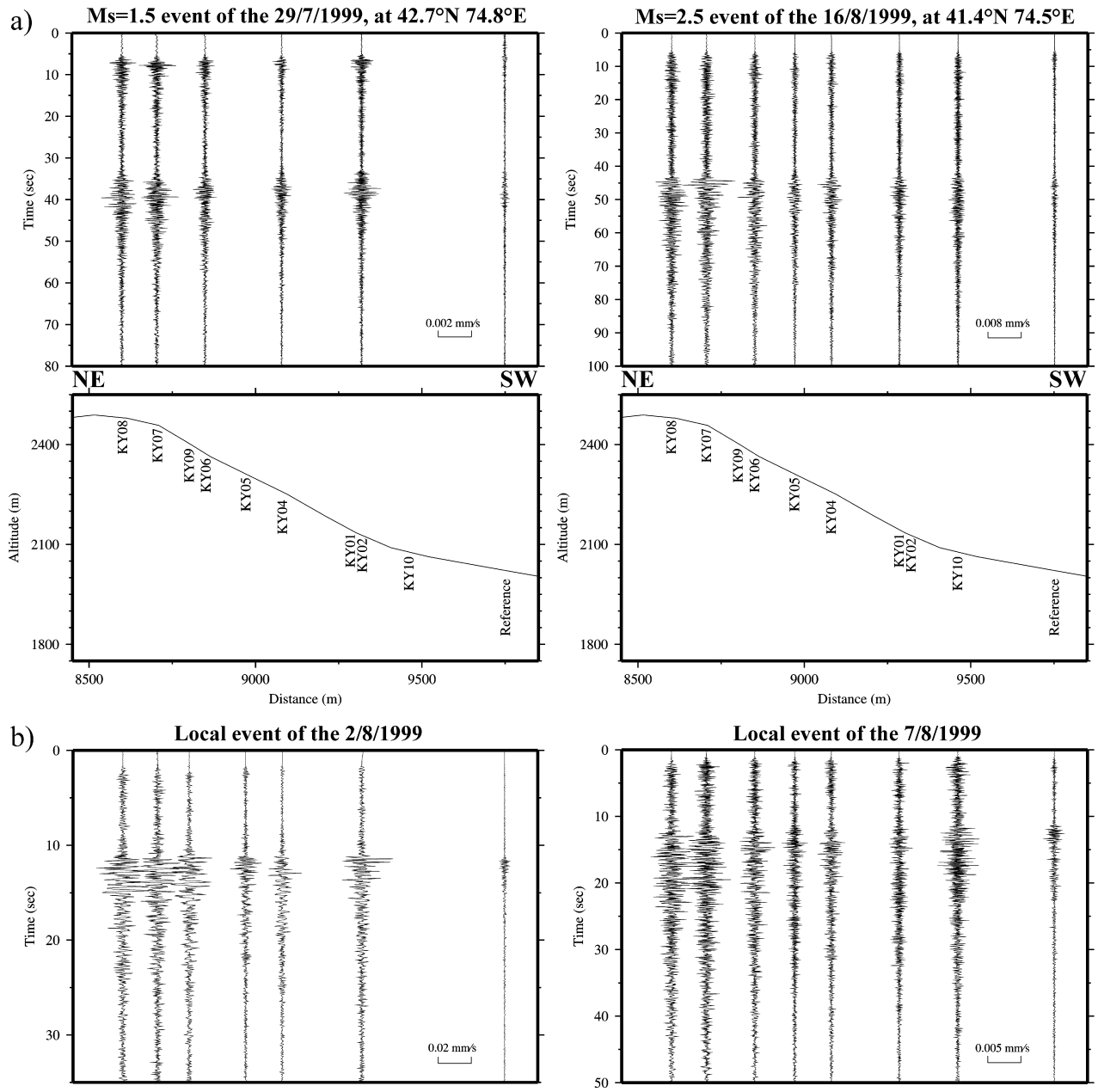

Figure 6. (a) Recordings (N–S component) of two regional events on the landslide site (KY01 to KY10) and at Ananevo station (reference). The positions of stations KY01 to KY10 are projected on a NE–SW profile along the western slope (part of section 1 in Fig. 6c). The position of the reference station has been moved for better presentation. (b) Recordings (N–S component) of two local events on the landslide site (KY01 to KY10) and at Ananevo station (reference).

the transfer functions, and 3D computations were carried out.

The 3D FE models were built using spectral elements only in order to save computational costs but with the consequence that flexibility of construction is more limited. Thus, the two upper surface layers were combined into one (layer 1′ in Table 2) with Vs of 600 m/sec, which is a mean value between 400 and 910 m/sec weighted for varying thickness. Also, geometries with strongly varying thickness were smoothed in order to avoid element distortion. The implications of these two main modifications are discussed in the following.

As input, an E–W oriented, 0.012 m/sec amplitude Ricker wavelet of 2 Hz was used. Results for the 3 km (SSW–NNE) by 2.4 km (WNW–ESE) and by 3 km (Z) model with two surface layers are shown in terms of maximum amplitude and SSR distributions (Fig. 12). From Figure 12a, it can be seen that highest amplitudes affect the area in the vicinity

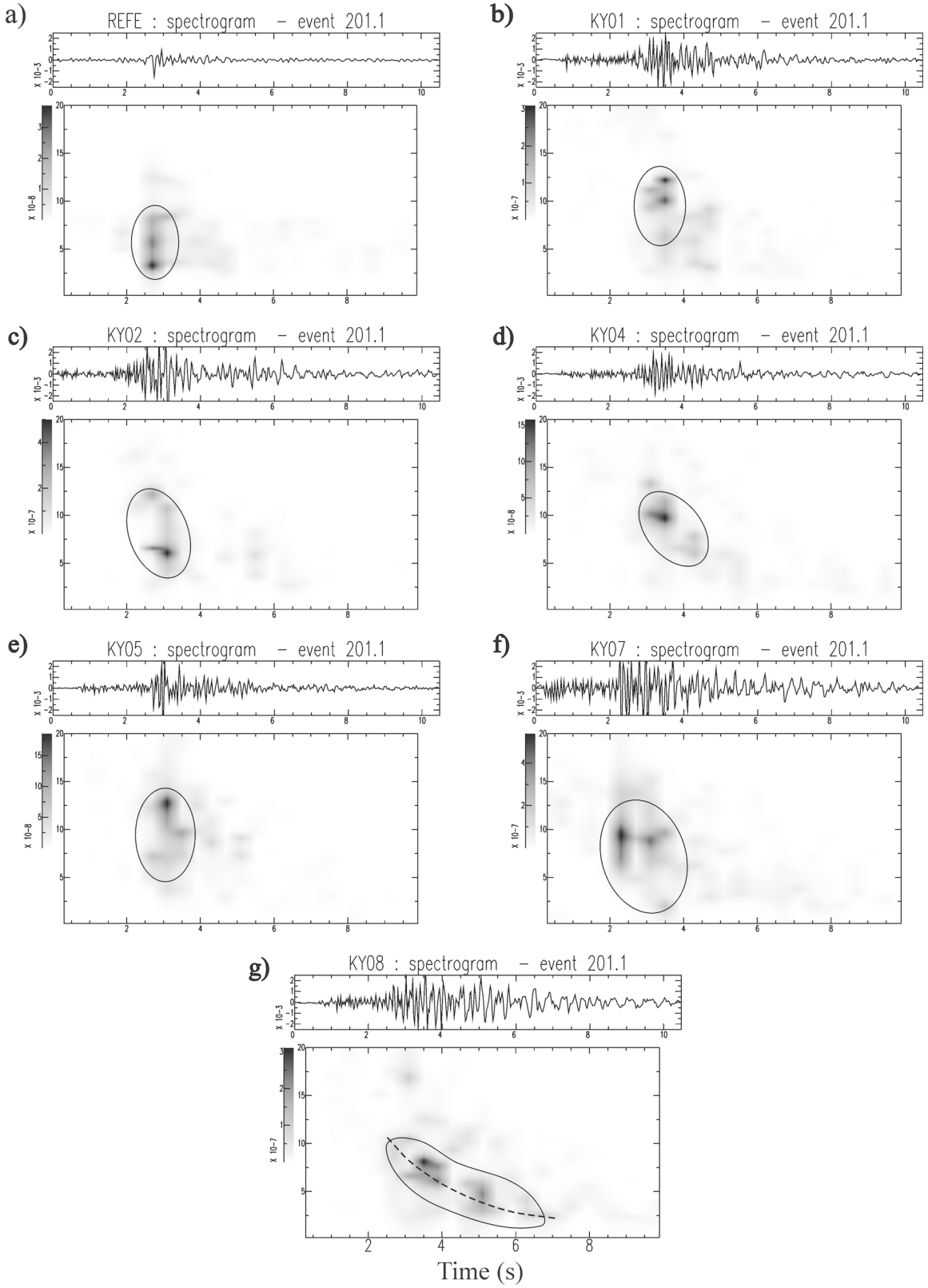

Figure 7. (a–g) Seismograms (N–S component) and normalized spectrograms (frequency along vertical axis and time along horizontal axis) of a local event (07/20/1999) recorded at stations REFE (reference), KY01, KY02, KY04, KY05, KY07, and KY08 respectively. For all stations maximum seismic energy is roughly outlined.

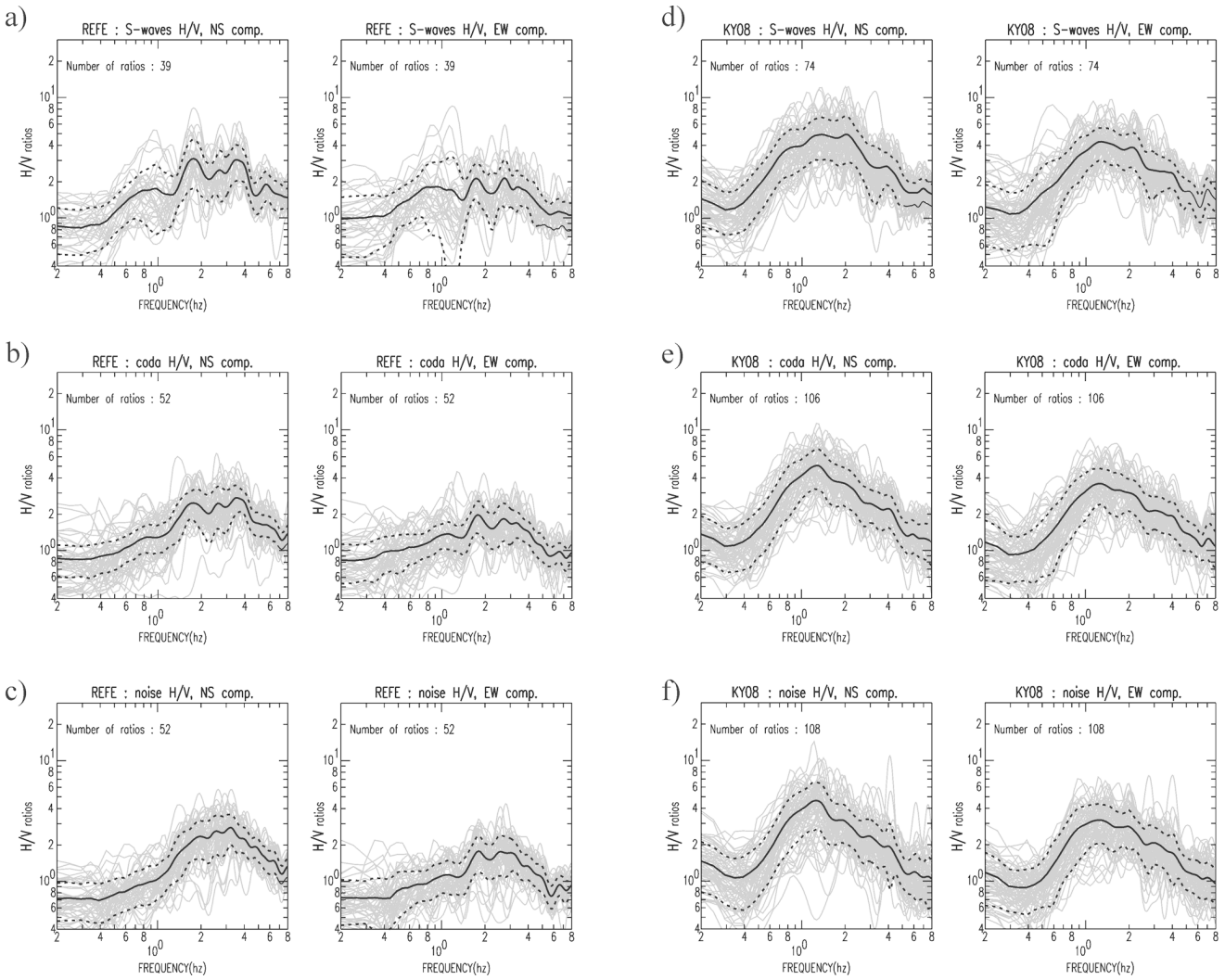

Figure 8. H/V ratios (for regional events) of N–S and E–W components for stations REFE (reference station at Ananevo) and KY08 (at the mountain crest). Station REFE: (a) H/V ratios (gray line) for 15-sec *S*-wave windows of 39 regional events with mean (black solid line) and ± one standard deviation curves (black dashed line). (b) H/V ratios (gray) for 20-sec coda windows of 52 events with mean (solid) and ± one standard deviation curves (dashed). (c) H/V ratios (gray) for 52 20-sec noise windows with mean (solid) and ± one standard deviation curves (dashed). Station KY08:(d) H/V ratios (gray) for 15-sec *S*-wave windows of 74 regional events with mean (solid) and ± one standard deviation curves (dashed). (e) H/V ratios (gray) for 20-sec coda windows of 106 events with mean (solid) and ± one standard deviation curves (dashed). (f) H/V ratios (gray) for 108 20-sec noise windows with mean (solid) and ± one standard deviation curves (dashed).

of the scarp and along the mountain crest. Lowest amplitudes are at least twice the amplitude (0.025 m/sec, Fig. 12b) obtained at the reference receiver location (Fig. 12a) in the homogeneous bedrock model. The reference receiver signal was also used for the computation of the SSR in Figure 12b and c. Besides the higher amplification level shown by these SSRs, the general distribution of site effects along the NE–SW and E–W profiles is similar to the one predicted in 2D: highest amplification affects the top of the mountain and the resonance frequency increases downhill. The lowest fundamental frequency, above the scarp, is somewhat higher (1.8) for the 3D model than the value obtained in 2D and by the experimental data (1.1–1.3 at KY07). This probably results from the combination of the two upper layers.

The computed results are compared with corresponding experimental data in terms of spectral ratios (Fig. 13). In the same figure are also added 1D transfer function calculated with the method of Kennett (1983) on the basis of the 1D-velocity log below each station inside the geophysical model (Fig. 5).

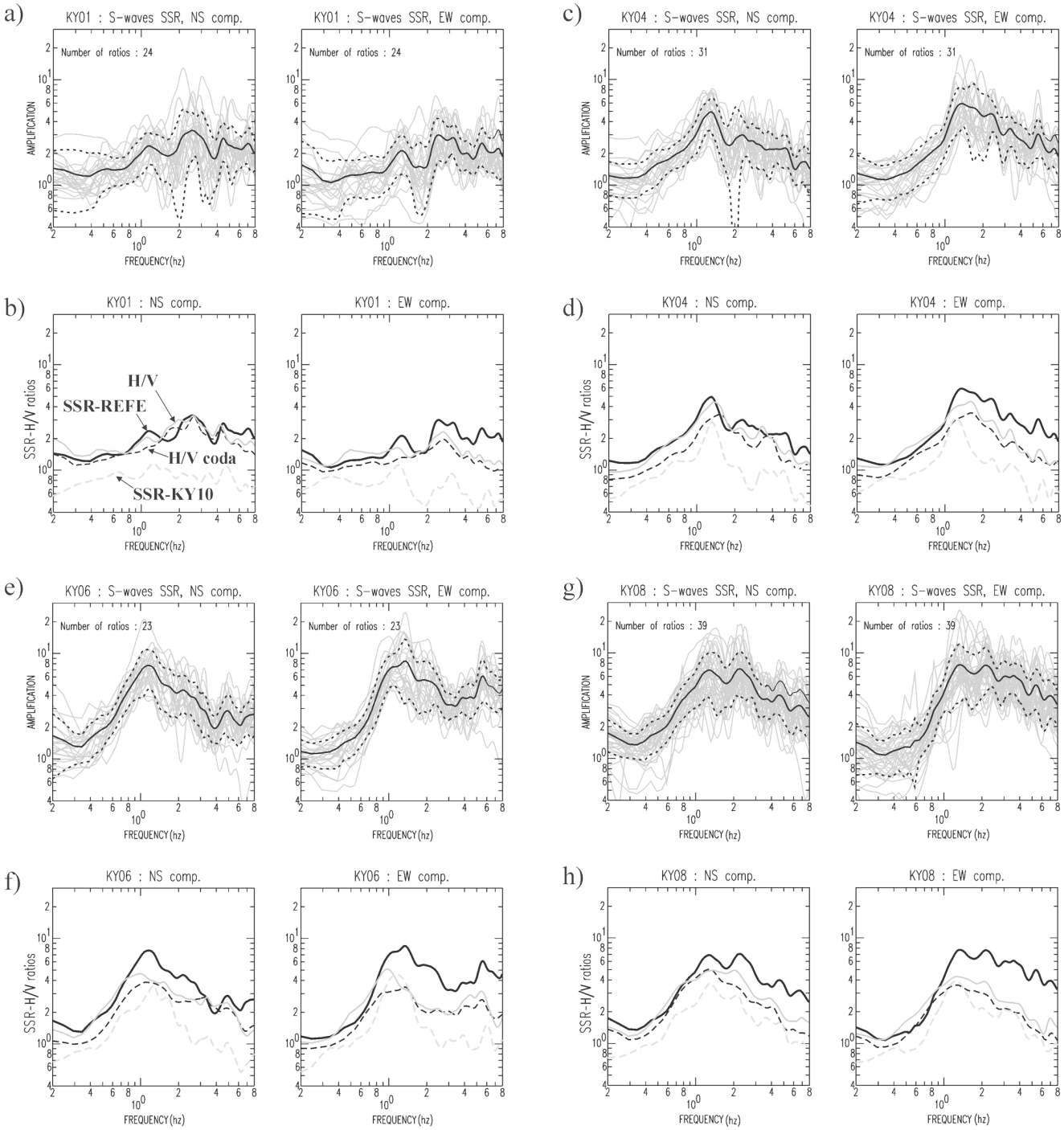

Figure 9. Comparison between SSR and H/V ratios (regional events) for four stations along the western slope: N–S and E–W component SSR ratios (gray lines, reference station Ananevo, REFE) and mean SSR (black solid line) ± one standard deviation curves (black dashed line) of events recorded at stations (a) KY01, (c) KY04, (e) KY06, and (g) KY08. Comparison between mean SSR (black solid line, reference station REFE), mean SSR (dashed light gray line, reference station KY10), mean H/V ratio over 15-sec *S*-wave windows (solid gray line) and H/V ratio over 20-sec coda windows (dashed dark gray line) for stations (b) KY01, (d), KY04, (f), KY06, and (h) KY08.

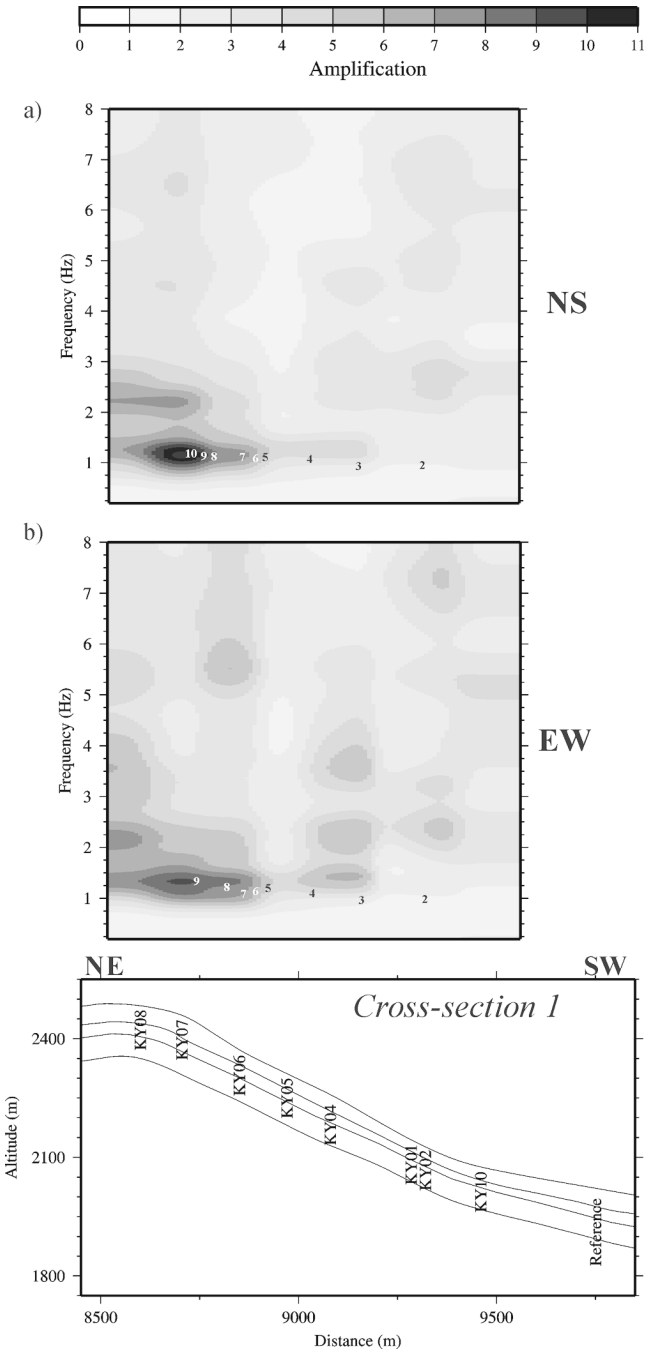

Figure 10. (a) Distribution of N–S component SSR along the southwestern slope of the landslide mountain. (b) Distribution of E–W component SSR along the southwestern slope of the landslide mountain.

First, Figure 13a shows the theoretical 2D SSR computed for cross section 1 with bedrock and surface layers in relation to the 1D transfer function and experimental SSR (N–S component) at corresponding sites along the slope. At the foot of the hill (stations KY10 and KY02), theoretical 2D ratios show the main features of the observations. 1D and 2D transfer functions along and at the top of the slope reproduce a slight shift of the fundamental frequency but do, in general, not compare well with experimental ratios. Even though they are simpler, spectral 1D modeling results (section 1, Fig. 12a) are relatively similar to the 2D modeling ones, except at the foot of the slope where the fundamental frequency is shifted to higher values. Cross section 2 runs perpendicular to the crest, outside the main orientation (N–S) of the almost linear seismic array. Therefore theoretical 2D SSR obtained in this section with bedrock and surface layers are compared only with experimental SSRs (EW component) at corresponding sites around the crest (stations KY06, KY07, and KY09), with the 1D transfer function and 3D SSR (Fig. 13b). 3D SSR are not compared with the N–S component results obtained along the NE–SW profile because the input and motion was oriented E–W. In terms of fundamental resonance frequency, theoretical 2D and 3D ratios are a closer fit to the experimental ones, while 1D computations yield higher values corresponding to the second peak of modeled 2D SSR. At the crest station (KY07), 2D and 3D theoretical amplifications are larger than experimental mean ratios, whereas 1D amplification is similar to the observed one. To both sides of the crest, at stations KY06 and KY09, observed maximum amplifications are more or less fit by the theoretical 1D, 2D, and 3D spectral ratios (at a different frequency).

A common characteristic of all types of modeling results and of the experimental data is the shift of the resonance frequency along the southwestern slope. Because the 1D computations are also able to show this tendency, a 1D effect (i.e., related to thickness variation only) can be considered as a primary cause of observed site effects. This interpretation was checked by sensitivity analyses using the Monte-Carlo method (Field and Jacob, 1993). For each station, 500 computations of the 1D transfer function were performed by varying (normal distribution between extremes $-$ mean $\pm$ 20% of mean parameter values) the thickness parameters of the three surface layers and the four *S*-wave velocities (three surface layers and bedrock, see Table 2) in order to take the uncertainty into account. Results for the different stations were similar and hint to a clear dependency of 90% of the 1D fundamental frequency variation on the ratio between the Vs and the thickness of the first layer (Vs of 400 m/sec). Lower fundamental frequencies in the crest region can therefore be linked to the larger thickness of the surficial weathered layer, such as it has been shown by the geophysical data.

1D effects cannot, however, explain entirely the observed site effects in, both, the time and frequency domains. In general, 1D computations neither produce the duration of the motion nor the SSR shape with amplification over a wide frequency range. Particularly, the results along the E–W profile reveal that 1D transfer functions do not compare well with amplification between 1 and 2 Hz, that is, in the range of the first resonance frequency at stations along the crest. The first peak at 1–1.5 Hz at station KY07 is best reproduced by the 2D simulations along cross section 2, while SSR at

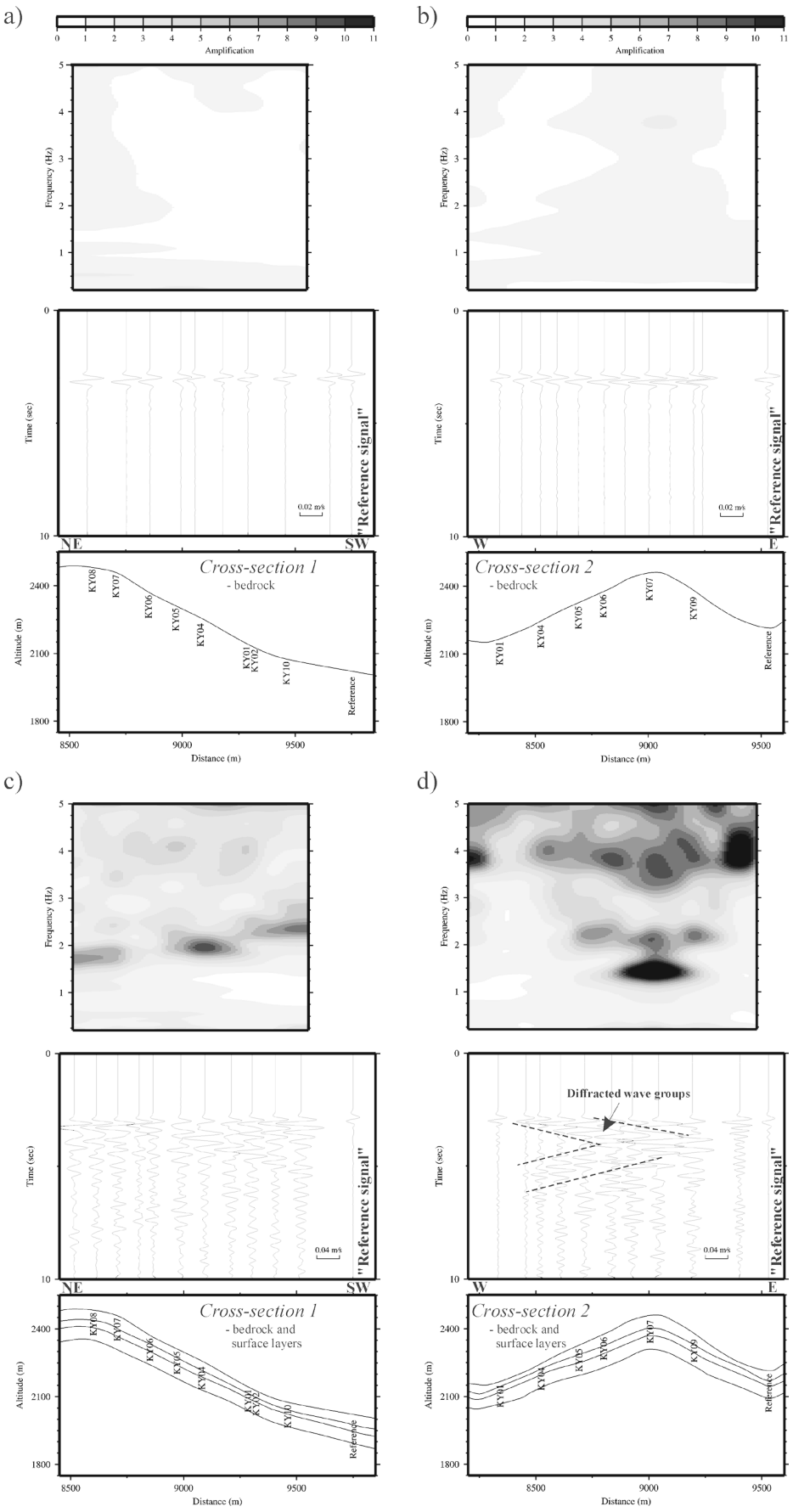
a)
b)
c)
d)
Amplification
Frequency (Hz)
Time (sec)
"Reference signal"
0.02 m/s
0.04 m/s
NE
SW
W
E
Cross-section 1
- bedrock
Cross-section 2
- bedrock
- bedrock and surface layers
Altitude (m)
Distance (m)
KY01
KY02
KY04
KY05
KY06
KY07
KY08
KY09
KY10
Reference
Diffracted wave groups

Figure 11. Numerically simulated time histories (velocities, m/sec) and SSR distributions obtained at the surface of four different models: Cross sections (a) 1 and (b) 2 with homogeneous bedrock (amplitude scale: 0.02 m/sec); cross sections (c) 1 and (d) 2 with bedrock and surface layers (amplitude scale: 0.04 m/sec). The reference signal in cross sections 1 and 2 with bedrock with surface layers is the same as in cross sections 1 and 2 only composed of homogeneous bedrock. In cross section 1, the reference receiver lies 2 km southwest of the foot of the slope; in section 2, the reference receiver lies 2 km west of the foot of the slope. Groups of diffracted waves are indicated in (d).

stations KY06 and KY09 are better fitted by corresponding 3D results. Thus, amplification at the crest below 1.5 Hz can be explained by a 2D effect, which seems to depend on the ridgelike topography combined to the strong thinning of the first surface layer toward the valley bottoms. The relative misfit of the 3D SSR in this regard can be explained by differences in the model structure. First, the Vs value of 600 m/sec used in 3D simulations and weighted for varying thickness is too high for zones with a thick upper layer, for example, the mountain crest, and slightly too small for zones with a thinner surface layer, for example, lower part of slopes. This effect partly explains the higher fundamental frequencies at the mountaintop in the 3D model with respect to the 2D model. Secondly, the strong lateral thinning of the upper layer along the E–W profile implicates diffraction effects that can generate additional low-frequency surface waves focusing in the crest region and inducing amplification in the low-frequency range. These diffracted waves seem to be more pronounced in 2D than in 3D simulations (compare Figs. 11d and 12c) because of the stronger thickness variation in the 2D model. On the other side, the smoother geometry with a less confined zone in the crest region used in 3D allows a better fit of SSR at KY06 and KY09.

A major 3D effect proved by respective numerical results and the experimental data is the wide amplified frequency range. This ground-motion characteristic appears to be related to the clear 3D geometry of the site (Fig. 12a), that is, a N–S trending crest limited by a south-facing scarp.

Both 2D and 3D SSR significantly overestimate experimental SSR at about 2 Hz for sites along the mountain crest (Fig. 13b). Alternatively, the latter might also be underestimated at this frequency because the reference station is clearly affected by amplification effects (see H/V ratios in Fig. 8) in the range between 1.5 and 4 Hz. Taking into account a factor of 2 at 2 Hz, actual amplification would be about 12, such as produced by 2D and 3D modeling.

In conclusion, comparison between theoretical and experimental results contributed to determine significant parameters of the observed ground-motion characteristics: the presence of weathered low-velocity surface layers, the thinning or wedging of the upper surface layer downhill and the 3D ridge-scarp structure: The strong and significant effect of the layer geometry was also confirmed by 2D and 3D modeling with a model composed of one average layer (Vs of 1200 m/sec) overlying the bedrock. These simulations produced smaller amplification ratios (less than 10) occurring at higher frequencies (above 2.5 Hz). On the other hand, 3D simulations with a two-layer structure and an upper layer Vp of 400 m/sec instead of 600 m/sec clearly overestimate the average amplification level, especially in the low-frequency domain.

From the point of view of morphology, the 3D ridge-scarp structure implicates an important role of the scarp, a feature that was not present prior to the slope failure in 1911. 3D numerical results for the same model built with the assumed initial topography showed, however, that the scarp itself is not a key factor (see Havenith *et al.*, in press). Instead, these additional computations revealed that the ending of the ridge by a triangular-shaped south-facing slope plays a similar confining role as the scarp. By there, it could also be concluded that longitudinal cross sections 1 and 3 have a very similar ground motion response (Havenith *et al.*, in press).

Discussion and Conclusions

In this article we present the results of a geophysical and seismological survey on a rockslide in Kyrgyzstan, triggered by the 1911 Kemin earthquake. In order to set up the background for the seismic trigger mechanisms, experimental and numerical studies of ground-motion dynamics were undertaken. Geophysical investigations consisting of seismic refraction tests coupled with inversion of surface waves were used to build a 3D seismic model of the site including three surface layers and bedrock. Although the geology of the site was supposed to be homogeneous granite, geophysical data indicated the presence of shallow low-velocity layers (Vs of 250–400 m/sec) with increasing thickness (30–50 m) toward the mountain crest. Seismological data collected on the site and by a permanent seismological station at Ananevo were analyzed in terms of spectrograms, H/V ratios, and standard spectral ratios. The spectrograms indicated that energy at low frequency (around 1 Hz) is generally focused in the crest region.

Comparison between H/V ratios over noise, coda, and *S*-wave windows as well as SSR over *S*-wave windows (using two reference stations) has consistently indicated the same fundamental frequency at a specific site. Moreover, H/V ratios calculated for different wave types exhibit a very stable shape on both horizontal components. The H/V curves are very close to the amplification function calculated by the SSR method below the resonance frequency of the site. Above this frequency, H/V ratios are systematically lower than the SSR. This inequality has been observed for a large number of sites over the world, although some exceptions exist (for a review, see Bard [1999]). H/V ratios at Ananevo

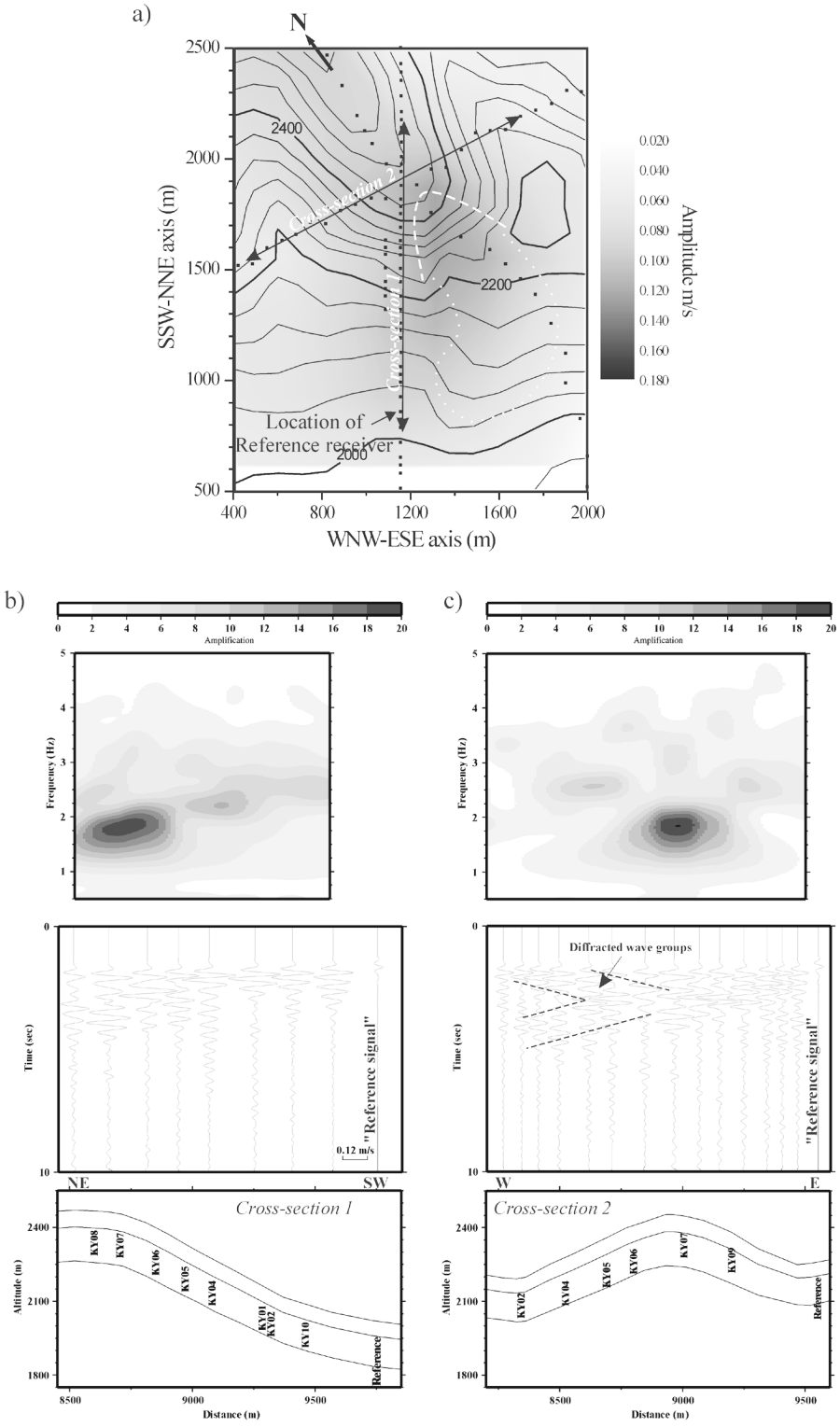

Figure 12. (a) Distribution of maximum amplitudes over the surface of the 3D FE model. The scarp and the geometry of the tongue are marked by a dashed white line and a dotted white line, respectively. The location of the reference receiver in the bedrock model is shown. (b) Time histories (velocities, m/sec) and SSR distributions (amplification scale with maximum of 20, different from the one in Fig. 11 limited at 11) obtained at the surface of model: cross sections (b) 1 and (c) 2 (see location in Figure 12a) with bedrock and surface layers (amplitude scale: 0.12 m/sec). Groups of diffracted waves are indicated in (c).

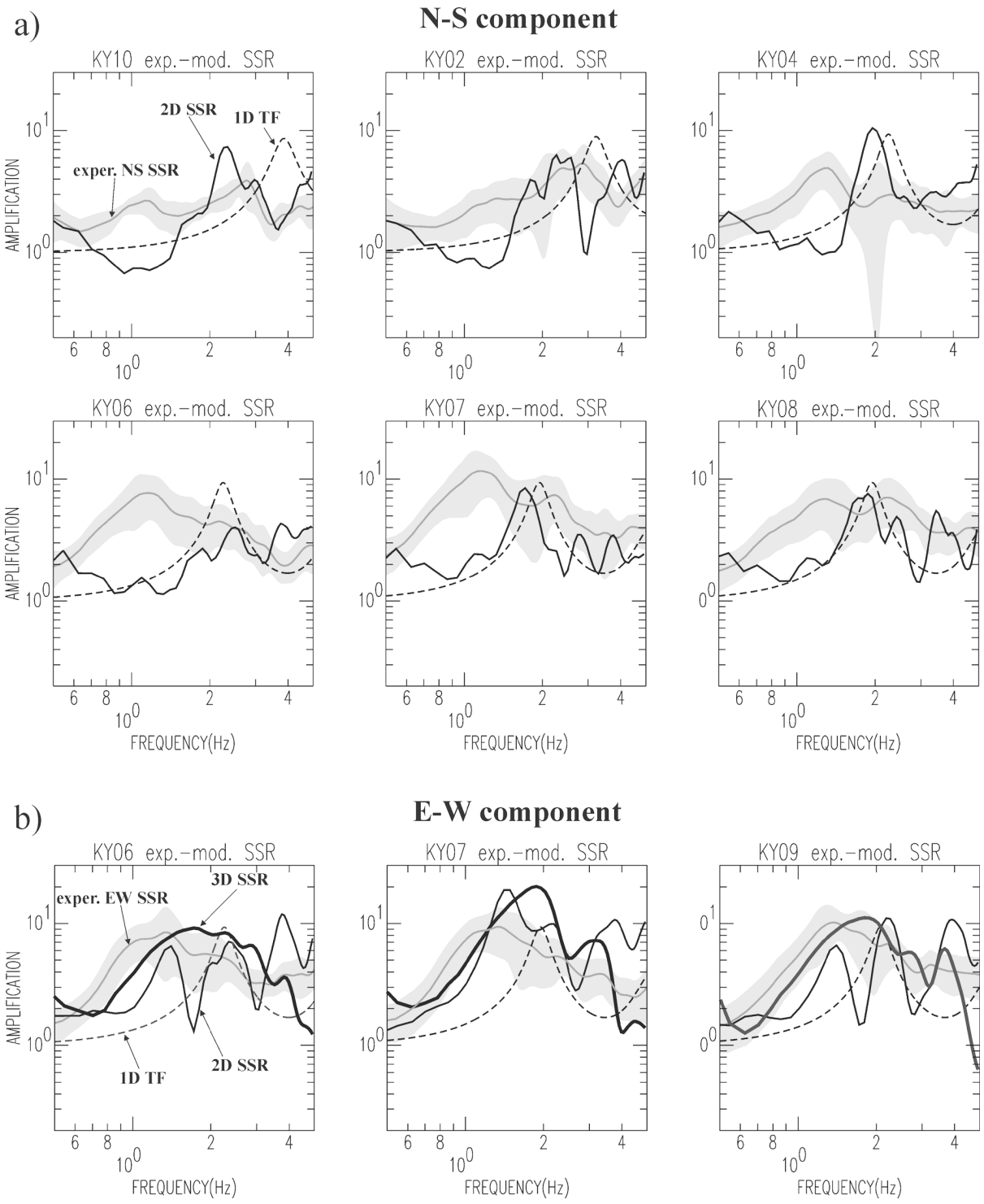

Figure 13. (a) Modeled 1D transfer function (1D TF, dashed black line) and theoretical 2D SSR in cross section 1 with bedrock and surface layers (2D SSR, solid black line) compared with experimental N–S component SSR (experimental N–S SSR, solid gray line, ± one standard deviation, area with gray fill) at corresponding sites along the slope, (stations KY10, KY02, KY04, KY05, KY06, KY07 and KY08). (b) 1D TF (dashed black line), 2D SSR (solid black line), and 3D SSR (thick black line) obtained along cross section 2 with bedrock and surface layers (solid gray line) compared with experimental E–W SSR (solid gray line, ± one standard deviation, area with gray fill) at corresponding sites around the crest, (stations KY06, KY07, and KY09).

seem also able to provide a rough estimate of the shape of the amplification curves, which is not generally the case elsewhere (Bard, 1999). Distributions of SSR using a reference station located at 2.5 km from the rockslide clearly revealed strongly varying site effects over the area with highest amplification (larger than 10) on the crest of the hill and a shift of the fundamental frequency toward higher frequencies downhill. These two features were analyzed theoretically by 1D, 2D, and 3D modeling. All modeling tools were able to reproduce the frequency shift along the N–S slope. These results suggest that the resonance frequency shift can be satisfactorily accounted for with a 1D model and is linked to an increasing thickness of the first layer from foot to top of the slope. This relationship was established by the geophysical data and by the Monte-Carlo sensitivity analysis.

The large amplification at the crest between 1 and 2 Hz and the motion duration are, however, related to 2D or 3D geometry. Actually, the thinning of the upper layer downhill can be considered as not only responsible for changing 1D transfer functions, but also for generation of diffracted waves. Over and above that, the geometry of the ridge ending by a triangular slope combined with wedgelike surface layers geometry creates a confined zone, where the incoming waves are trapped. This is supported by the records from the crest stations showing increased signal duration linked to the generation of dispersive surface waves.

The analysis of the varying ground motion characteristics closely connected with the investigation of the subsurface geology highlighted the need of detailed geophysical information over a large area.

The presence of a deeply weathered rock layer of varying thickness all over the mountain then proved to be the most significant factor constraining local site effects. If not taken into account, the numerical modeling would systematically have underestimated the measured amplification level.

The question still remains open if the observed site effects might have influenced slope failure. In this regard, we undertook studies of the effect of site amplification on strain focusing in the elastic domain. Related results are presented by Havenith *et al.* (in press). Two further articles are in preparation, where additional structural and geotechnical information on the site is presented. These articles will analyze the influence of ground-motion dynamics on the plastic behavior of the slope and discuss various possible slope failure mechanisms.

Acknowledgments

The research leading to this article was funded by the European Community (EC, DG XII contract IC15-CT97-0202). We wish to thank Ivan, Abdirashid, Tulegen (KIS), Isaakbek, Yuri, and Vlad (GEOPRIBOR) of Bishkek, Kyrgyzstan; Cécile and Renaud (LGIT, Grenoble, France); Hervé (LGIH, Liège, Belgium); Damien (RMCA, Tervuren, Belgium); Alexander (Hydroproject I., Moscow, Russia); and Marco (Dip. Strutt., P. di Milano, Milan, Italy) for their help in the field or in the lab. We particularly are grateful to Denis Hatzfeld (LGIT, Grenoble, France), who allowed us to using their seismological stations, as well as to Steve Roecker (Rensselaer Polytechnic Institute, New York) for sending us data of the Ananevo seismological station.

References

Abdrakhmatov, K. Y., S. A. Aldazhanov, B. H. Hager, M. W. Hamburger, T. A. Herring, K. B. Kalabaev, V. I. Makarov, P. Molnar, S. V. Panasyuk, M. T. Prilepin, R. E. Reilinger, I. S. Sadybakasov, B. J. Souter, Y. A. Trapeznikov, V. Y. Tsurkov, and A. V. Zubovich (1996). Relatively recent construction of the Tien Shan inferred from GPS measurements of present-day crustal deformation rates, *Nature* **384,** 450–453.

Aitmatov, I. T., I. A. Torgoev, and Y. G. Alioshin (1997). Monitoring of dangerous geodynamical areas, in *Proc. of the 30th International Geological Congress*, Beijing, China, 4–14 August, Vol. II and III, pp. 1–7.

Akad. Nauk Kirghiz S.S.R. and Ministry of Geology, U.S.S.R. (1980). Geological map of Kirghiz SSR, scale: 1:200,000.

Avouac, J. P., P. Tapponnier, M. Bai, H. You, and G. Wang (1993). Active thrusting and folding along the northern Tien Shan and late Cenozoic rotation of the Tarim relative to Dzungaria and Kazakhstan, *J. Geophys. Res.* **98,** no. B4, 6755–6804.

Bard, P.-Y. (1999). Microtremor measurements: a tool for site effect estimation? in *Proc. of the Second International Symposium on the Effects of Surface Geology on Seismic Motion*, Yokohama, Japan, December 1998, Vol. I–III, 1251–1279.

Bogdanovich, M. M. C., J. Kark, B. Korolkov, and D. Muchketov (1914). Earthquake of the 4th January 1911 in the northern districts of the Tien Shan, *Tr. Geol. Com. Ser.* **89,** 270 pp.

Borcherdt, R. D. (1970). Effects of local geology on ground motion near San Francisco Bay, *Bull. Seism. Soc. Am.*, **60,** 29–61.

Bouchon, M. and J. S. Barker (1996). Seismic response of a hill: the example of Tarzana, California, Bull. Seis. Am., 86, 66–72.

Burger, H. R. (1992). *Exploration Geophysics of the Shallow Subsurface*, K. G. Marshak (Editor), Prentice Hall, New York,

Cobbold, P. R., E. Sadybakasov, and J. C. Thomas (1996). Cenozoic transpression and basin development, Kyrgyz Tien Shan, Central Asia, in Geodynamics evolution of sedimentary basins, F. Roure, N. Ellouz, V. S. Shein, I. Skvortsov (Editors), Technip, Paris. pp. 181–202.

Delvaux, D., K. E. Abdrakhmatov, and A. L. Strom (2001). Landslides and surface breaks of the Ms 8.2 Kemin earthquake, Kyrgyzstan, *Russian Geology and Geophysics* (*Geologya i Geophysika*) **42,** 1167–1177.

Demanet, D. (2000). Tomographies 2D et 3D à partir de mesures géophysiques en surface et en forage, *Ph.D. Thesis*, Liege University, Belgium.

Faccioli, E., F. Maggio, R. Paolucci, and A. Quarteroni (1997). 2D and 3D elastic wave propagation by a pseudo-spectral domain decomposition method, *J. Seismology* **1,** 237–251.

Field, E. H., and K. H. Jacob (1993). Monte-Carlo simulation of the theoretical site response variability at Turkey Flat, California, given the uncertainty in the geotechnically derived input parameters, *Earthquake Spectra* **9,** 669–701.

Field, E. H., and K. H. Jacob (1995). A comparison and test of various site response estimation techniques, including three that are non reference-site dependent, *Bull. Seism. Soc. Am.* **85,** 1127–1143.

Gomez, J. M., B. Bukchin, R. Madariaga, E. A. Rogozhin and B. Bogachkin (1997). Rupture process of the 19 August 1992 Susamyr, Kyrgyzstan, earthquake, *J. Seismology* **1,** 219–235.

Havenith, H.-B., M. Vanini, D. Jongmans, E. Faccioli (2002). Initiation of earthquake-induced slope failure: influence of topographical and other site specific amplification effects—experimental data and numerical modeling, *J. Seismology* (in press).

Herrmann, R. (1987). *Computer Programs in Seismology*, Vol. VI, Saint Louis University, St. Louis, Missouri.

Imanbekov, S., K. Dzhanuzov, S. Uranova, and A. Frolova (1999). Seismic hazard and building vulnerability in Kyrgyzstan, in *Seismic Hazard and Building Vulnerability in Post-Soviet Central Asian Republics*, S. A. King, V. I. Khalturin, and B. E. Tucker (Editors), Kluwer, Hingham, Massachusetts, 93–105.

Jongmans, D., and P. E. Malin (1995). Microearthquake S-wave observations from 0 to 1 km in the Varian Well at Parkfield, California, *Bull. Seism. Soc. Am.* **85,** no. 6, 1805–1820.

Kennett, B. L. N. (1983). *Seismic Wave Propagation in Stratified Media*, Cambridge University Press, Cambridge.

Lacoss, R. T. (1971). Data adaptive spectral analysis methods, *Geophysics* **36,** 661–675.

McCann, D. M., and A. Forster (1990). Reconnaissance geophysical methods in landslide investigations, *Eng. Geol.* **29,** no. 1, 59–78.

Mellors, R. J., F. L. Vernon, G. L. Pavlis, G. A. Abers, M. W. Hamburger, S. Ghose, and B. Illiasov (1997). The Ms = 7.3 1992 Suusamyr, Kyrgyzstan earthquake. I. Constraints on fault geometry and source parameters based on aftershocks and body wave modeling, *Bull. Seism. Soc. Am.* **87,** 11–22.

Nakamura, Y. (1989). A method for dynamic characteristics estimation of subsurface using microtremors on the ground surface, *Quarterly Rept. RTRI* **30,** 25–33.

Paolucci, R., E. Faccioli, and F. Maggio (1999). 3D response analysis of an instrumented hill Matsuzaki, Japan, by a spectral method, *J. Seismology* **3,** 191–209.

Pavlis, G. L., V. Schulte-Pelkum, S. Roecker, and F. Vernon (2000). Polarization and phase velocity anomalies of teleseismic P phases in the Central Tien Shan, *EOS* **81,** no. 48.

Reigber, C, D. Angermann, G. W. Michel, J. Klotz, R. Galas, and the CATS-team (1999). New constraints on the distribution of deformation in Central Asia: GPS results covering the Tien Shan, N-Pamir and Tarim', in *Proc. of 24th General Assembly on Geophysical Research*, The Hague, The Netherlands, Vol. 1, 39 pp.

Riepl, J., P.-Y. Bard, D. Hatzfeld, C. Papaioannou, and S. Nechtschein (1998). Detailed evaluation of site response estimation methods across and along the sedimentary valley of Volvi (EURO-SEISTEST), *Bull. Seism. Soc. Am.* **88,** 488–502.

University of Liege (LGIH)
Sort Tilman-Batiment B19
4000 Liege, Belgium
HB.Havenith@ulg.ac.be
(H.B.H., D.J.)

Université Joseph Fourier (LIRIGM)
BP53-38041
Grenoble cedex 9, France
(D.J., P.Y.B.)

Dipartimento di Ingeneria Strutturale
Politecnico di Milano
20133 Milan, Italy
(E.F.)

Kyrgyz Institute of Seismology
Bishkek, Kyrgyzstan
(K.A.)

LCPC Paris, France
(P.Y.B.)

Manuscript received 23 July 2001.